Acta Cryst. (1992). **A48**, 575-591

Parametrization of Triply Periodic Minimal Surfaces. II. Regular Class Solutions

By A. Fogden and S. T. Hyde

Department of Applied Mathematics, Research School of Physical Sciences, Australian National University, Box 4, Canberra 2601, *Australia*

(*Received* 6 *June* 1991; *accepted* 4 *March* 1992)

Abstract

A derivation is given of the set of triply periodic minimal surfaces of monoclinic symmetry and higher that fall within the regular class (including those containing self-intersections). The Gauss maps, Weierstrass parametrizations and asymmetric units of each surface are included. Triclinic relatives of monoclinic surfaces are also discussed. Some minimal surfaces that lack translational order but exhibit orientational symmetry also naturally appear within this derivation.

Introduction

In the first paper in this series (Fogden & Hyde, 1992) we have established necessary conditions for the existence of infinite (triply) periodic minimal surfaces (IPMS) within the regular class. These constraints are imposed on the Weierstrass functions [(14) or the modified form (15) of the previous paper, here denoted (I14) and (I15), respectively*], which lead to the IPMS *via* the Weierstrass representation. We now derive the IPMS in the regular class that are consistent with these constraints.

1. Global Riemann surface structure

(*a*) *Plane lines of curvature and linear asymptotes*

The set of branch-point distributions listed in Table I2 (Fogden & Hyde, 1992) represents all IPMS candidates generated from Schwarz triangle tilings. The assessment of each candidate involves investigation of the Riemann surface covering of the unit sphere corresponding to the branch-point distribution and, specifically, the continuous subregions that tessellate the Riemann surface. As observed in the preceding study (Fogden & Hyde, 1992) such a subregion must comprise a union of the underlying Schwarz triangles and is thus termed a (generalized) geodesic polygon. If such a polygon exists for which the bounding (geodesic) edges may be consistently identified as images of plane lines of curvature or linear asymptotes then the distribution gives rise to an IPMS, with the smallest such polygon representing the Gauss-map image of the IPMS *Flächenstück*. From this Gauss-map image the reconstruction of the *Flächenstück* is straightforward. Crystallographic considerations of the *Flächenstück*, with reference to its bounding cell, then determine whether continuation of the surface element yields a true IPMS or generates self-intersections.

Existence of an IPMS for a particular branch-point distribution is thus related to the existence of a globally consistent network of image segments of plane lines of curvature and/or linear asymptotes on the underlying Schwarz tiling of the Riemann surface. These special arcs are the Schwarz triangle edges for which the Weierstrass function satisfies the necessary conditions derived in the previous paper (Fogden & Hyde, 1992). Global consistency then requires the compatibility of the Schwarz tiling and the Weierstrass function in simultaneously reconciling these necessary conditions on each branch of the Riemann surface. We now formulate these requirements.

Consider a general surface-normal vector imaged at infinity in the complex plane and a ray segment emanating at an angle φ from a point lying over it on one of the s sheets of the Riemann surface. This ray corresponds to a plane line of curvature or linear asymptote provided the condition

$$\exp(-i4\varphi)R[\exp(-i2\varphi)\bar{\omega}] = \pm\bar{R}(\omega) \qquad (1)$$

derived from (I23) is satisfied for that branch of the Weierstrass function $R(\omega)$. For the regular class of IPMS the number of sheets $s = \text{l.c.m.}\,\{b_i + 1\}_{i=1}^{n}$ is the least common multiple (l.c.m.) of the local Gauss-map degrees at the branch points, with the s branches of the Weierstrass function defined by $\exp(i\psi_p)R$ such that $\psi_p = (2\pi/s)p$, $p = 0, \ldots, s-1$, where R is given by the form (I14) or (I15) subject to the constraint (I10). Recall that, with $(b+1)$ denoting the local Gauss-map degree at this general surface-normal vector, on the Riemann surface above the corresponding image point the s sheets are pinned in groups of $(b+1)$ at the $s/(b+1)$ such branch points of order $b \geq 0$. We label these $s/(b+1)$ branch points with the index r and the s sheets with the index p introduced above. Then the $(b+1)$ sheets pinned at the rth branch point are identified with the

---

* The numeral I indicates an equation or table of the first paper in this series (Fogden & Hyde, 1992).

0108-7673/92/040575-17$06.00

© 1992 International Union of Crystallography

$(b+1)$ values of p giving remainder r on division by $s/(b+1)$. Thus the local branch-point structure partitions the set of s values of p into equivalence classes modulo $s/(b+1)$ of $(b+1)$ points,

$$\begin{aligned}\langle r\rangle &= \{p : r = p \bmod s/(b+1)\}\\ &= \{[s/(b+1)]m + r,\quad m = 0, \dots, b\},\\ & r = 0, \dots, s/(b+1) - 1. \end{aligned}\tag{2}$$

The corresponding $(b+1)$ Weierstrass function values $\exp(i\psi_p)R$ in the vicinity of the rth branch point are then given by $\exp(i\psi_r)\exp[i2m\pi/(b+1)]R$. In this way each sheet is locally assigned an integer pair r and m such that r labels the branch point and m distinguishes the $(b+1)$ sheets pinned there.

Substituting equations (I14) or (I15) subject to the constraint (I10), for the range of angles $0 \le \varphi_r < 2\pi(b+1)$ tracing the $(b+1)$ sheets of the Riemann surface pinned at the rth branch point, the corresponding function $\exp(i\psi_r)R$ satisfies (1) only if the necessary branch-point symmetry condition

$$\{\overline{\exp(i\varphi_r)\omega_i}\} = \{\exp(i\varphi_r)\omega_i\}, \qquad b_i \text{ constant} \tag{3}$$

is supplemented by the condition

$$\exp\{i2[\varphi_r(b+2)/(b+1) + \psi_r]\} = \pm 1. \tag{4}$$

As expected, this pair of equations reverts to (I27)–(I28) for the case $r = 0$ considered in the analysis of the previous paper. So the spectrum of images of plane lines of curvature and linear asymptotes on the Riemann surface emanating from the rth branch point are the geodesic arcs at the angles in the set

$$\begin{aligned}\varphi_r &= [(b+1)/(b+2)][m_r\pi/2 - (2\pi/s)r],\\ & m_r = 0, \dots, 4(b+2) - 1, \end{aligned}\tag{5}$$

about which the branch-point distribution is symmetric (where the parity of m_r distinguishes the two types of curve).

With the branch-point distribution generated from a single underlying tile, the set of geodesic arcs about which this distribution is symmetric is precisely the set of tile edges over which the branch points are propagated by reflection (as opposed to composition of this operation with reflection in any existing internal symmetry axes of the tile). Thus the network of images of plane lines of curvature and linear asymptotes is generated by the subset of these tile edges for which the angles subtended are consistent with those permitted by (5). We now determine this subset.

Suppose that the general surface-normal vector considered above is imaged at a point on a tile boundary that is a reflection axis of the distribution. Let $\lambda\pi$ denote the smallest angle between reflection axes at this point. If the point lies on an edge then $\lambda\pi = \pi$, otherwise the point is situated at a vertex and $\lambda\pi$ is the vertex angle of the tile (or twice this value if the other tile edge meeting there is not a reflection axis). Then at the rth of the $s/(b+1)$ branch points of order b lying over this point on the Riemann surface, the family of images of plane lines of curvature or linear asymptotes meeting there correspond to the subset of angles φ_r in (5) that are multiples of this underlying tiling angle $\lambda\pi$, *i.e.* $\varphi_r = n_r\lambda\pi$. From (5) the permissible set of integer multiples n_r must satisfy

$$n_r\lambda = [(b+1)/(b+2)](m_r/2 - 2r/s). \tag{6}$$

Defining the greatest common divisor

$$\begin{aligned} G &= \text{g.c.d.}[(1/\lambda)(b+1), 2(b+2)]\\ &= \begin{cases} \text{g.c.d.}[(1/\lambda), 2(b+2)] & \text{if } b \text{ is even}\\ 2\text{g.c.d.}[(1/\lambda), (b+2)] & \text{if } b \text{ is odd} \end{cases}, \end{aligned}\tag{7}$$

(6) possess integral solutions n_r and m_r provided r is an element of the set

$$\begin{aligned} S = \{r = 0, \dots, s/(b+1) - 1:&\\ s \text{ divides } (4/\lambda)(b+1)r/G\}& \end{aligned}\tag{8}$$

{of which $r = 0\ [\bmod s/(b+1)]$ is one such member}. Hence only those of the $s/(b+1)$ branch points (labelled with the index r) for which r is contained in this set S possess images of plane lines of curvature or linear asymptotes meeting there. For those that do, the general solution of (6) is then

$$\begin{aligned} n_r &= [(1/\lambda)(b+1)/G]q - [(4/\lambda)(b+1)/sG]rn_r^0,\\ m_r &= [2(b+2)/G]q - [(4/\lambda)(b+1)/sG]rm_r^0\\ &\qquad (q \in \mathbf{Z}), \end{aligned}\tag{9}$$

where (n_r^0, m_r^0) is any particular integral solution of the equation

$$2(b+2)n_r^0 - (1/\lambda)(b+1)m_r^0 = G. \tag{10}$$

So the family of such curves emanating from the rth branch point (if r is an element of S) on the $(b+1)$ sheets pinned there is given by the family of angles $\varphi_r = n_r\lambda\pi$ modulo $2\pi(b+1)$, generated by $2G$ consecutive values of the integer q in (9).

Equations (6)–(10) specify the local structure required of the images of plane lines of curvature and linear asymptotes on the Riemann surface above a particular point on a tile reflection boundary, commensurate with the boundary angle $\lambda\pi$ subtended there. The underlying tiling then ensures that the required local structure may be simultaneously satisfied at all such boundary points, for each of the solutions of equation (I37) listed in Table I2. Hence in each case there exists a consistent network of these image arcs on the Riemann surface (such that points related by symmetry possess local structures related by the same symmetry). This implies the existence of a generating circuit, from which the entire network may be obtained *via* symmetry operations of the branch-point distribution.

Existence of a corresponding IPMS demands that the smallest generating circuit bounds a region comprising an equivalent fraction of the Riemann surface, which is then identified with the Gauss-map image of the *Flächenstück*. Such an identification is possible if this circuit is simply connected on the Riemann surface. Hence the determination of those members of the solution set in Table I2 giving rise to IPMS involves application of this criterion to the network of images of plane lines of curvature and linear asymptotes thus constructed. For those that do, this direct method immediately yields the *Flächenstück* of the IPMS.

(*b*) *Rotation and roto-inversion symmetries*

Having fully specified the plane line of curvature and linear asymptote structure of the surfaces derived from solutions in Table I2, it remains to classify the rotation and roto-inversion symmetries of those surfaces satisfying the closure criterion derived above.

Consider first pure rotational symmetry. Under this symmetry operation the surface is mapped onto itself under clockwise rotation through an angle φ' about the z axis if the condition

$$\begin{pmatrix} x \\ y \\ z \end{pmatrix}(\exp[-i\varphi']\omega) = \begin{pmatrix} \cos\varphi' & \sin\varphi' & 0 \\ -\sin\varphi' & \cos\varphi' & 0 \\ 0 & 0 & 1 \end{pmatrix}\begin{pmatrix} x \\ y \\ z \end{pmatrix}(\omega), \tag{11}$$

equivalent to (I30), is satisfied. On substitution of the representation (I1) this geometrical condition reduces to the functional equation

$$\exp[-i2\varphi']R(\exp[-i\varphi']\omega) = R(\omega). \tag{12}$$

For the regular class of IPMS the solution of this equation yields the criteria (I31)-(I33) governing the perpendicular rotational symmetry of the surface about a particular point of order $b \geq 0$ that, with respect to the chosen orientation, has a vertical normal vector imaged at infinity in the closed complex plane. Further, if this z-axis direction coincides with that of a labyrinth axis of the minimal surface then (12) gives the rotational-symmetry angle of the surface about this line. In general, for the Weierstrass functional form (I15) [in conjunction with the constraint (I10)] to obey this equation, the necessary condition (I31) must be satisfied simultaneously with the equation

$$\exp\{i[\varphi'(b+2)/(b+1) + \Delta\psi_r]\} = 1, \tag{13}$$

[where, as previously, $\psi_r = (2\pi/s)r$, $r = 0, \ldots, s/(b+1) - 1$] or equivalently

$$\varphi' = [(b+1)/(b+2)][2m'\pi - (2\pi/s)\Delta r] \quad (m' \in \mathbf{Z}). \tag{14}$$

The factor $\exp(i\Delta\psi_r)$ is introduced here to account for the possibility that, in passing from ω to $\exp(-i\varphi')\omega$, the corresponding Weierstrass-function value passes (continuously) on the Riemann surface from a sheet pinned at the rth branch point of order b over the point at infinity to a sheet pinned at the r'th such branch point (where $\Delta r = r' - r$). For the case of perpendicular rotation about the flat point of order b under consideration, $\Delta r = 0$, hence the previous result (I33) is recovered and the basic rotational-symmetry angle $\varphi'/(b+1)$ on the surface is $[1/(b+2)]2\pi$. On the other hand, traversal of the Riemann surface induced by rotation about the labyrinth axis parallel to this flat-point normal vector through an angle φ' satisfying (I31) is inaccessible with respect to the local branch-point structure above this normal-vector image. Hence in this case $\Delta r \neq 0$ and the off-surface angle of rotational symmetry in real space is the minimum value of φ' in (14) consistent with the symmetry angle of the branch-point distribution and the known Δr value.

We now address the roto-inversions. Since the representation (I1) is specific to the arbitrary choice of normal-vector orientation applied to the minimal surface (*i.e.* to the choice of colouring of the two sides), the distinction must be made between off-surface and on-surface roto-inversion symmetries. Consider first a general off-surface roto-inversion. The surface is imaged to itself on composition of a clockwise rotation of φ'' about the z axis with inversion in the origin provided

$$\begin{pmatrix} x \\ y \\ z \end{pmatrix}(-\exp[-i\varphi'']/\bar{\omega}) = -\begin{pmatrix} \cos\varphi'' & \sin\varphi'' & 0 \\ -\sin\varphi'' & \cos\varphi'' & 0 \\ 0 & 0 & 1 \end{pmatrix}\begin{pmatrix} x \\ y \\ z \end{pmatrix}(\omega), \tag{15}$$

which reduces to

$$(1/\omega^4)\,\overline{\exp[-i2\varphi'']R(-\exp[-i\varphi'']/\bar{\omega})} = R(\omega). \tag{16}$$

This relation is in turn satisfied for an IPMS in the regular class if the branch-point distribution possesses this symmetry, that is, the polar branch points (lying above the origin and the point at infinity in the complex plane) have equal order, *i.e.* $b_1 = b_n = b \geq 0$, with the finite nonzero branch points having the property

$$\{-\exp[-i\varphi'']/\bar{\omega}_i\} = \{\omega_i\}, \qquad b_i \text{ constant}, \tag{17}$$

and, further, if

$$\exp[i(\pi - \varphi'')(b+2)/(b+1)] = \prod_{i=2}^{n-1} \omega_i^{b_i/(b_i+1)}. \tag{18}$$

Thus in general the angle of roto-inversion symmetry of the surface about a labyrinth axis coinciding with the z axis and inversion point situated at the origin is the minimal-value solution φ'' of (18), if it exists. For the special case in which $\varphi''=\pi$ the twofold roto-inversion reduces to on-surface mirror symmetry in the plane $z=0$, with the subsequent condition

$$\prod_{i=2}^{n-1} \omega_i^{b_i/(b_i+1)}=1, \qquad (19)$$

which recalls the previous criterion for a plane line of curvature, derived from the positive root of (I25) on setting $n_1=n_2=0$.

The criterion for on-surface symmetry at a surface point of order b with vertical normal vector under rotation of φ''' about this normal line (the z axis) and inversion in the point (imaged at the origin) is obtained by negating the right-hand sides of (11)-(13), in conjunction with the necessary condition (I31). This yields the condition

$$\exp\{i[\varphi'''(b+2)/(b+1)+\Delta\psi_r]\}=-1, \qquad (20)$$

where now, as distinct from the on-surface rotational symmetry case, $\Delta r\neq 0$ and consequently $b>0$. Hence on-surface roto-inversion is exhibited at this (flat) point if (20) possesses a solution consistent with branch-point structure; the basic rotation angle $\varphi'''/(b+1)$ then corresponding to the minimal such value. Note in particular that if $\exp(i\Delta\psi_r)=-1$ then the composite symmetry decouples into rotational symmetry at angle φ' and inversion symmetry.

Finally, consider the orientation-preserving composite symmetry of twofold rotation about the y axis followed by clockwise rotation of φ about the z axis, for which the condition is

$$\begin{pmatrix} x \\ y \\ z \end{pmatrix}(-\exp[-i\varphi]/\omega) = \begin{pmatrix} -\cos\varphi & \sin\varphi & 0 \\ \sin\varphi & \cos\varphi & 0 \\ 0 & 0 & -1 \end{pmatrix}\begin{pmatrix} x \\ y \\ z \end{pmatrix}(\omega). \qquad (21)$$

Via the representation (I1) the associated Weierstrass functional equation is

$$(1/\omega^4)\exp[-i2\varphi]R(-\exp[-i\varphi]/\omega)=R(\omega). \qquad (22)$$

The regular-class functional form is a solution of (22) provided $b_1=b_n=b\geq 0$ and the remaining branch points satisfy

$$\{-\exp[-i\varphi]/\omega_i\}=\{\omega_i\}, \qquad b_i \text{ constant}, \qquad (23)$$

subject to

$$\exp[i(\pi-\varphi)(b+2)/(b+1)]=\prod_{i=2}^{n-1}\omega_i^{b_i/(b_i+1)}. \qquad (24)$$

Note that this latter constraint is identical to (18), the analogous constraint for off-surface rotation-inversion symmetry.

2. Regular-class solutions for the Schwarz triangles

The analytical apparatus assembled in the first section facilitates the 'reconstruction' of a minimal surface in the regular class from its corresponding branch-point distribution. We now apply this procedure to the branch-point sets listed in Table I2, thus yielding explicitly the regular IPMS related to Schwarz triangle tilings. Recall that each such set containing branch points on triangle edges and/or faces gives rise to a number of distribution types (that is, symmetry-distinct configuration classes).

Branch-point distributions that are consistent with the closure criterion stated in the preceding section are represented, with reference to their underlying Schwarz tiling, in Figs. 1(a)-17(a). The numbering of the figures follows the grouping of the solution sets in Table I2, ordered with decreasing tiling symmetry from Schwarz case 4 solutions to those of Schwarz case 1, $n=2$. For example, in the Schwarz case 1, $n=3$ group, the solution set $\{0,4,4\}$ is found to be incompatible with the closure criterion, while the set $\{\{0,0,1\},\{1\},\Phi\}$ admits three possibilities satisfying this requirement - given in Figs. 11(a), 12(a) and 13(a). In the latter two cases the branch points are propagated by reflection over all three edges, with the pair distinguished by the choice of two symmetrically different edges to which the branch point may be assigned. In Fig. 11(a), however, continuation across the unit circle is defined by the composition of reflections in the unit circle and the ray bisecting the triangle.

The corresponding Weierstrass functions for the branch-point distributions are obtained by substitution of the sets of branch-point sites $\{\omega_i\}_{i=1}^n$, together with their orders, into the relevant functional form (I14) or (I15). The sets $\{\omega_i\}_{i=1}^n$ are, in turn, determined as follows.

The two solutions arising from Schwarz case 4, given in Figs. 1(a) and 2(a) (for which the only possible symmetry operations defining branch-point propagation over each tile boundary are edge reflections), lead to branch points at the $\pi/3$ and $\pi/4$ vertices of the tessellation, situated at the set of eight and six points $\{[(3^{1/2}\pm 1)/2^{1/2}]\exp(iM\pi/2)\colon M\in\mathbf{Z}\}$ and $\{0,\infty,\exp(i\pi/4)\exp(iM\pi/2)\colon M\in\mathbf{Z}\}$ respectively (for this orientation).

The remaining solutions pertain to Schwarz case 1, for which a general point ω, interior to a tile with polar angle π/n, possesses $4n$ images in the tesselated complex plane. If the branch points are propagated by edge reflection then these images are the group generated by the three reflection operations $\omega\to\bar\omega$, $\omega\to\exp(i2\pi/n)\bar\omega$, $\omega\to 1/\bar\omega$,

$$\langle\bar\omega, \exp(i2\pi/n)\bar\omega, 1/\bar\omega\rangle = \{\{\omega,\bar\omega,1/\omega,1/\bar\omega\}\exp(i2M\pi/n)\colon M\in\mathbf{Z}\}.$$

The degenerate case in which a generator is rendered

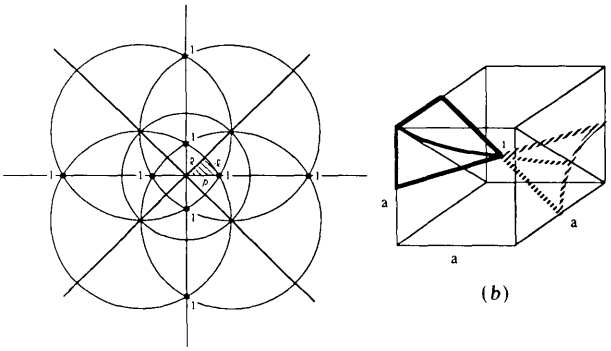

(a) (b)

Fig. 1. The D and P surfaces.

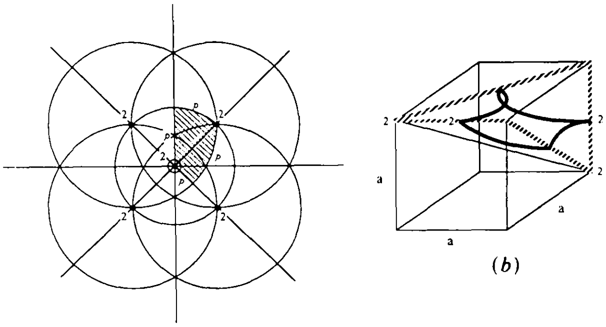

(a) (b)

Fig. 2. The I-WP and Stessman surfaces.

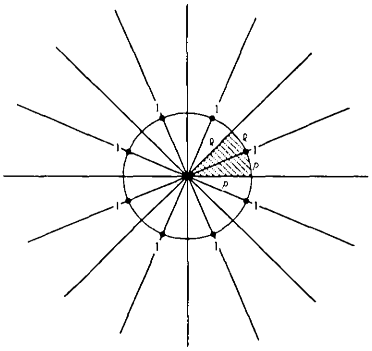

(a)

Fig. 3. The self-adjoint special case of the CLP family (see Fig. 9).

Figs. 1–20. The 'regular' minimal surfaces derived here. The figures (a) give the branch-point distribution in the complex plane, relative to its stereographically projected spherical tessellation. Filled circles indicate branch points, whose orders are given by the adjacent numeral. Larger open circles centred on the origin denote a branch point at the point at infinity. The shaded region is the projected Gauss-map image of the *Flächenstück*, corresponding to the Weierstrass function in Table 1. The labels 'p' and 'ℓ' indicate images of *Flächenstück* boundaries that are plane lines of curvature and linear asymptotes, respectively. The geometry in $\mathbf{R}^3$ of the *Flächenstück* is illustrated by the solid lines in figures (b), with the adjoint *Flächenstück* given in broken lines, and the symbolic names of both are given in each caption (in this order), unless otherwise stated. (The notation conventions are detailed in § 2.) Each of the surfaces is described in the text and the relevant crystallographic information is summarized in Table 2.

an identity gives a set of $2n$ edge points. Thus the image set of $\omega \in \mathbf{R}$ [respectively $\exp(i\pi/n)\mathbf{R}$] is $\{\{A, 1/\bar{A}\}\exp(i2M\pi/n)\colon M \in \mathbf{Z}\}$, where $A \in \mathbf{R}$ [respectively $\exp(i\pi/n)\mathbf{R}$], while $|\omega| = 1$ yields the set $\{\{\exp(i\theta), \exp(-i\theta)\}\exp(i2M\pi/n)\colon M \in \mathbf{Z}\}$, where $0 \le \theta < 2\pi$. Double degeneracies in turn produce the set of n vertices at $\exp(i2M\pi/n)$ or $\exp[i(2M+1)\pi/n]$. On the other hand, if unit-circle reflection is replaced by composition of this operation with reflection in the internal-symmetry axis $\arg\omega = \pi/2n$ of the tile then the $4n$ generic images are

$$\begin{aligned}&\langle\bar{\omega}, \exp(i\pi/n)(1/\omega)\rangle\\ &\quad = \{\{\omega, \bar{\omega}, (1/\omega)\exp(i\pi/n),\\ &\qquad (1/\bar{\omega})\exp(i\pi/n)\}\exp(i2M\pi/n)\colon M \in \mathbf{Z}\}.\end{aligned}$$

In this case there exists only two degenerate cases, both consisting of $2n$ points. If $\omega \in \mathbf{R}$ then the above set reduces to $\{\{A, (1/A)\exp(i\pi/n)\}\exp(i2M\pi/n)\colon M \in \mathbf{Z}\}$, while $\omega = \exp(i\pi/n)(1/\omega)$ generates the special points $\exp[i(2M+1)\pi/2n]$.

These cases exhaust the image sets of all types of branch-point positions occurring in the solutions under all possible edge-propagation operations. The Weierstrass functions associated with the branch-point distributions in Figs. 1(a)–17(a) are trivially calculated from the above and are listed in the correspondingly numbered rows 1–17 of Table 1.

In each case the Riemann surface of the Weierstrass function is visualized as s superposed copies of the single sheet illustrated in Figs. 1(a)–17(a), pinned at the branch points according to the conventions described above. The Riemann surface is generated by repeated edge reflection of the geodesic polygon shaded in the figure, representing the smallest such unit bounded by images of plane lines of curvature (p) and/or linear asymptotes (ℓ). The tessellation gives the complete family of these special surface-curve images on the Riemann surface, specified by (6)–(10). It is geometrically apparent from the diagram that each of these cases satisfies the closure criterion, since this network of images clearly defines a consistent geodesic polygon.

Since the shaded region is the projected Gauss-map image of the *Flächenstück*, this information is sufficient, in conjunction with the symmetry analysis in § 1(b) above, to construct its form in $\mathbf{R}^3$. The plane lines of curvature and linear asymptotes defining the *Flächenstücke* are illustrated relative to their bounding cells for these cases by the solid-line curves in the corresponding figures marked (b). The symmetry of these examples ensures that these geodesic arcs form a closed circuit about the faces and/or edges of the bounding cell, in which case the form of the resulting *Flächenstück* is obvious. In other examples (treated in § 4 below), these arcs do not close up, however the form of the resulting *Flächenstück* can be deduced from the Gauss map.

Table 1. *Weierstrass functions corresponding to the Flächenstücke with Gauss-map image given in Figs.* 1(*a*)-20(*a*)

Figure no.	Weierstrass function $R(\omega)$
1	$(\omega^8-14\omega^4+1)^{-1/2}$
2	$[\omega(\omega^4+1)]^{-2/3}$
3	$(\omega^8+1)^{-1/2}$
4	$[\omega(\omega^6+1)]^{-1/2}$
5	$(\omega^6+1)^{-2/3}$
6	$\omega^{-3/4}(\omega^5+1)^{-1/2}$
7	$\omega^{-1/2}(\omega^4+1)^{-3/4}$
8	$[\omega^8-(A^4+1/A^4)\omega^4+1]^{-1/2}$: $0<A<1\Rightarrow A^4+1/A^4>2$
9	$(\omega^8-2\cos 4\theta\omega^4+1)^{-1/2}$: $0<\theta<\pi/4\Rightarrow -2<2\cos 4\theta<2$
10	$\omega^{-7/8}(\omega^3+1)^{-3/4}$
11	$\{\omega[\omega^6+(-A^3+1/A^3)\omega^3-1]\}^{-1/2}$: $0<A<1\Rightarrow -A^3+1/A^3>0$
12	$\{\omega[\omega^6-(A^3+1/A^3)\omega^3+1]\}^{-1/2}$: $0<A<1\Rightarrow A^3+1/A^3>2$
13	$[\omega(\omega^6-2\cos 3\theta\omega^3+1)]^{-1/2}$: $0<\theta<\pi/3\Rightarrow -2<2\cos 3\theta<2$
14	$\{\omega^8-[(A^2+1/A^2)-(B^2+1/B^2)]\omega^6-[(A^2+1/A^2)(B^2+1/B^2)-2]\omega^4-[(A^2+1/A^2)-(B^2+1/B^2)]\omega^2+1\}^{-1/2}$: $0<A, B<1$
15	$[\omega^8-2(\cos 2\theta_1+\cos 2\theta_2)\omega^6+2(2\cos 2\theta_1\cos 2\theta_2+1)\omega^4-2(\cos 2\theta_1+\cos 2\theta_2)\omega^2+1]^{-1/2}$: $0<\theta_1<\theta_2<\pi$
16	$[\omega^8-2(1+1/\lvert\omega_0^2\rvert^2)\,\mathrm{Re}\,(\omega_0^2)\omega^6+\{4(1/\lvert\omega_0^2\rvert^2)[\mathrm{Re}\,(\omega_0^2)]^2+\lvert\omega_0^2\rvert^2+1/\lvert\omega_0^2\rvert^2\}\omega^4-2(1+1/\lvert\omega_0^2\rvert^2)\,\mathrm{Re}\,(\omega_0^2)\omega^2+1]^{-1/2}$: $\omega_0\in\mathbf{C}$
17	$\omega^{-1/2}(\omega^4-2\cos 2\theta\omega^2+1)^{-3/4}$: $0<\theta<\pi/2\Rightarrow -2<2\cos 2\theta<2$
18-20	$(\omega^8-t_1\omega^6+t_2\omega^4-\bar{t}_1\omega^2+1)^{-1/2}$ where $t_1=\sum_{i=1}^{4} z_i^2$, $t_2=\sum_{\substack{i,j=1\\ i<j}}^{4} z_i^2 z_j^2$

	z_1^2	z_2^2	z_3^2	z_4^2
18	$\exp(i2\theta_1)$	$\exp(i2\theta_2)$	$\exp(i2\theta_3)$	$\exp(i2\theta_4)=\exp[-i2(\theta_1+\theta_2+\theta_3)]$
19	$r^2\exp(i2\theta)$	$(1/r^2)\exp(i2\theta)$	$\exp(i2\theta_3)$	$\exp(i2\theta_4)=\exp[-i2(2\theta+\theta_3)]$
20	$r_1^2\exp(i2\theta_1)$	$(1/r_1^2)\exp(i2\theta_1)$	$r_2^2\exp(i2\theta_2)=r_2^2\exp(-i2\theta_1)$	$(1/r_2^2)\exp(i2\theta_2)=(1/r_2^2)\exp(-i2\theta_1)$

The $\theta=\pi/2$ adjoint *Flächenstück* of the Bonnet family (obtained by introducing a multiplicative factor of *i* to the Weierstrass functions) is illustrated in each case by the broken-line curves in these figures. It is derived from the original Gauss-map image by simply interchanging the plane line of curvature and linear asymptote labelling.

The *Flächenstück* is not given in cases (such as Fig. 3*a*) where the branch-point distribution exhibits extra symmetries with respect to a generic distribution in that family (given in Fig. 9*a*), but for which the surface possesses no additional real-space symmetries. Further, the adjoint *Flächenstück* is not given in cases for which it is either identical to the original surface on reorientation, *i.e.* 'self-adjoint' (such as Fig. 17*b*), or, more generally, defines a continuous family of surfaces identical to that of the original (for example, Fig. 9*b*).

For the special members $\theta=0$ and $\theta=\pi/2$ of the Bonnet associate family, the existence of a particular IPMS implies the existence of lower-symmetry IPMS families derived by crystallographic distortion. The number of derivative-surface families of reduced symmetry is given by the number of possible distinct distortions of the original surface compatible with this symmetry. Each distortion represents an additional degree of freedom in the dimensions of the bounding cell corresponding to the introduction of a variable real parameter to the existing branch-point distribution and hence to the Weierstrass function. This study is limited to the regular class of IPMS, thus relatives of reduced symmetry of some listed

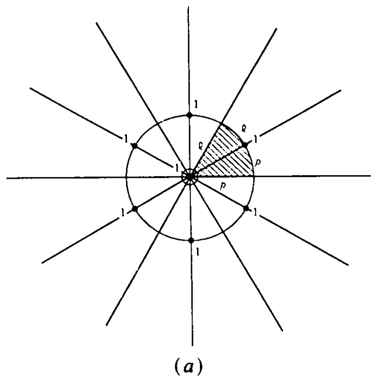

(*a*)

Fig. 4. The self-adjoint special case of the hCLP family (see Fig. 13).

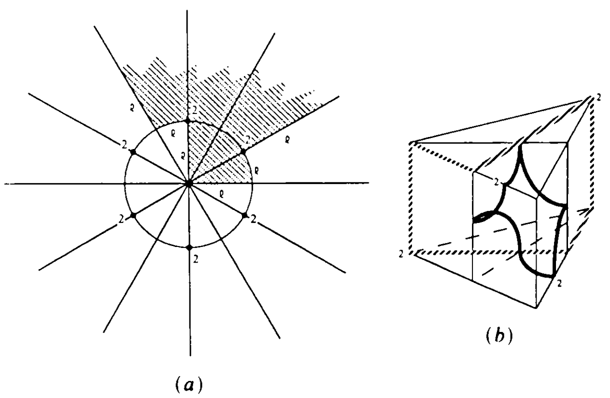

(*a*)

(*b*)

Fig. 5. The hI1 and hI1′ surfaces.

Table 2. *Summary of information for the minimal surfaces of Figs.* 1–20

The grouping of the cases indicates the sets of IPMS related by crystallographic distortion (with the third group mPCLP/mDCLP common to both of the first two sets). The space-group symmetry is not presented for the self-intersecting examples.

Minimal surface/ adjoint surface*	Space group	Genus†	Bicontinuous (intersection-free)	Table 1 entry	Figure no.
D/P	$Pn\bar{3}m - Fd\bar{3}m/Im\bar{3}m - Pm\bar{3}m$	3	√	1	1(*a*), (*b*)
rPD	$R\bar{3}m - R\bar{3}m$ $(c' = 2c)$	3	√	11	11(*a*), (*b*)
tD/tP	$P4_2/nnm - I4_1/amd/$ $I4/mmm - P4/mmm$	3	√	8	8(*a*), (*b*)
oPa/oDa	$Immm - Pmmm/Pnnn - Fddd$	3	√	16	16(*a*), (*b*)
oDb/oPb	$Cmma - Imma/Fmmm - Cmmm$	3	√	14	14(*a*), (*b*)
mPD	$C12/m1 - C12/m1$ $(c' = 2c)$	3	√	19	19(*a*), (*b*)
CLP/CLP‡	$P4_2/mcm - P4_2/mmc$ (v)	3	√	3	3(*a*)
CLP	$P4_2/mcm - P4_2/mmc$ (v)	3	√	9	9(*a*), (*b*)
oCLP′/oCLP	$Cmmm - Pmmm/Pccm - Cccm$	3	√	15	15(*a*), (*b*)
mCLP	$P12/m1 - P12/m1$ $(c' = 2c)$	3	√	18	18(*a*), (*b*)
mPCLP/mDCLP	$C12/m1 - P12/m1/$ $P12/c1 - C12/c1$ $(a' = 2a, b' = 2b)$	3	√	20	20(*a*), (*b*)/(*c*)
I-WP/Stessman	$Im\bar{3}m/$	4	√/×	2	2(*a*), (*b*)
VAL/VAL‡	$Cmma - Cmma$ $(c' = 2c)$	5	√	7	7(*a*)
VAL/VAL	$Cmma - Cmma$ $(c' = 2c)$	5	√	17	17(*a*), (*b*), (*c*)
H′/H	$/P6_3/mmc - P\bar{6}m2$	3	×/√	12	12(*a*), (*b*)
hCLP/hCLP‡		3	×	4	4(*a*)
hCLP		3	×	13	13(*a*), (*b*)
hI1/hI1′		4	×	5	5(*a*), (*b*)
hI2/hI2		9	×	10	10(*a*), (*b*)
pCLP/pCLP		5	×	6	6(*a*), (*b*)

* *S*/*S* denotes cases where the surface is self-adjoint up to reorientation. A single entry *S* denotes a self-adjoint family.

† This refers to the genus per lattice fundamental region for IPMS. In general (including noncrystallographic surfaces), the genus listed is that of the Riemann surface describing the surface. This is equal to $(1 + \text{l.c.m.}\{b_i + 1\})$.

‡ The branch-point distribution exhibits higher symmetry than that of the next entry.

surfaces (such as that in Fig. 2*b*) do not appear where the distortions result in an irregular branch-point distribution. In these cases only the most highly symmetric members of the family are 'regular'; the generic surface resides in the irregular class.

In the following subsection we discuss in detail the surfaces given in the figures – identifying those already known in the literature and analysing the new examples discovered here. Recall that the numbering of the figures follows the grouping of the possible branch-point sets listed in Table 12. In this way the procedure by which the surfaces are derived (and parametrized) is most clearly illustrated. The nature of the Weierstrass representation dictates that any systematic construction algorithm for IPMS be based upon considerations of the Gauss map. From this viewpoint the translational order (*i.e.* Euclidean tessellation) of an IPMS leads to orientational order in the Gauss map (*i.e.* spherical tessellation). As the latter is a necessary condition for the former – but not sufficient – our method ensures orientationally ordered minimal surfaces, although it cannot guarantee the existence of a 'true' IPMS for each case. Thus while minimal surfaces with compact *Flächenstücke* may be conveniently subdivided into three categories – true IPMS (free from self-intersections), IPMS possessing a finite number of self-intersections per translational unit cell, and noncrystallographic surfaces (lacking a translational unit) – the algorithm makes no distinction between these types. While application of the first surface category to structural description is well established, the second category is also relevant and arises naturally in modelling equipotential surfaces in charged arrays (for which self-intersections may occur naturally). For this reason all of the examples of these two types generated from the Schwarz tilings have been retained in the figures. We have also included one example of the third type arising from these solutions (*i.e.* orientational order only) – a 'quasi-crystalline' analogue of the more familiar true IPMS.

As a consequence of our listing of surfaces *via* their branch-point distributions, the sequencing of the figures does not lead to a grouping of surfaces with their lower-symmetry distortions. The full set of relations connecting the various surface families is quite intricate; the relations are explained below. The most important crystallographic data and relations resulting from this study are summarized in Table 2.

The scope of this study is limited to the $\theta = 0$ and $\theta = \pi/2$ surfaces in each Bonnet family. This is again a manifestation of our approach, since the Gauss map is invariant under this transformation and thus provides no direct insight into the possible existence of intermediate associate IPMS. Note though that, for the regular class of IPMS, the parameter range may be reduced to $0 < \theta < 2\pi/s$ without loss of generality since the s branches of the Weierstrass functional form (I14) or (I15) are defined by the factors $\exp(i\psi_p)$.

Description of the IPMS families

Fig. 1(*b*) gives the D surface and adjoint P surface of cubic symmetry discovered last century by Schwarz (1890). Stretching of the bounding cell in the vertical direction yields the tetragonal surface family pair tD(≡T) and tP, illustrated in Fig. 8(*b*) and analysed previously by Schoen (1970) and also by Lidin & Hyde (1987) and Lidin (1988). A further distortion of the tetragonal cell in either of the two perpendicular directions results in the two-parameter surface families oDa and oPa of Fig. 16(*b*), which are thus orthorhombic distortions of the original cubic surfaces (Fischer & Koch, 1989). Note that the corresponding distribution in Fig. 16(*a*) is the sole member of the Schwarz triangle solutions that possesses branch points within the triangle interiors. A circuit enclosing a single branch point of first order must

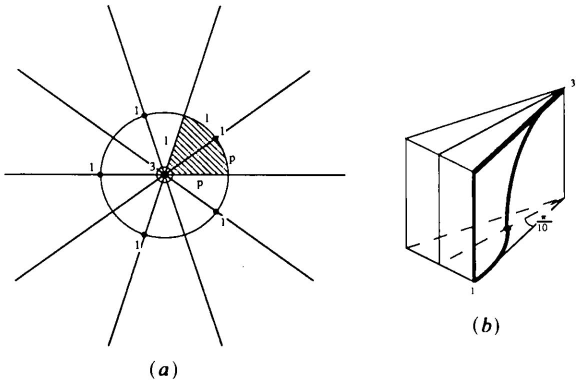

Fig. 6. The self-adjoint pCLP surface.

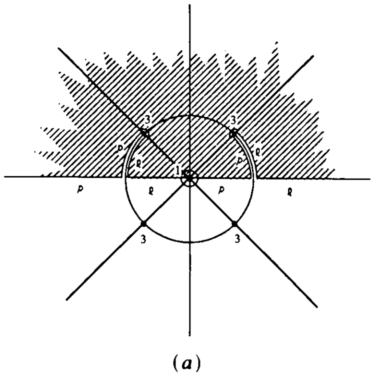

Fig. 7. The special case of the VAL surface (see Fig. 17).

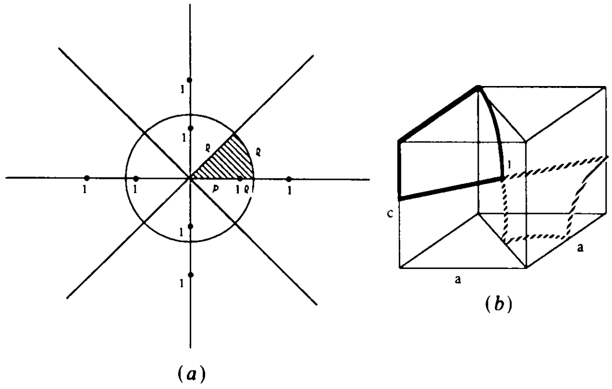

Fig. 8. The tD and tP surfaces.

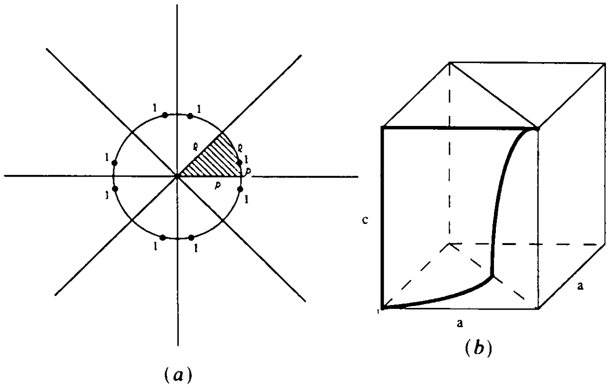

Fig. 9. The self-adjoint CLP family.

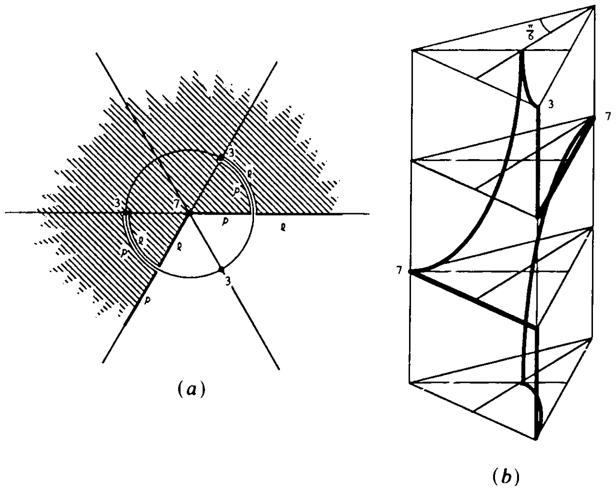

Fig. 10. The self-adjoint hI2 surface.

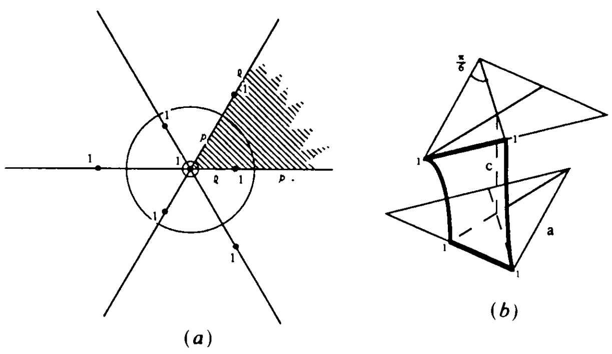

Fig. 11. The self-adjoint rPD family.

wind around twice on the pair of sheets of the Riemann surface pinned there. Accordingly in this case the continuous subregion of the Riemann surface representing the *Flächenstück* image is the pair of superposed copies of the first octant pinned at the interior branch point (denoted by the double shading and labelling in Fig. 16*a*).

A second pair of orthorhombic derivative families, oDb and oPb (displayed in Fig. 14*b*) exists, owing to the two distinct ways in which the tD and tP surfaces may be bounded by a parallelepiped unit (Fischer & Koch, 1989). On rhombohedral distortion of this pair of cubic surfaces the resulting family is self-adjoint, that is, D and P define the same one-parameter rhombohedral family, denoted rPD, given in Fig. 11(*b*) (Fischer & Koch, 1989). In all of these cases the Riemann surface is double sheeted so $s = 2$ and hence the genus $g = 3$.

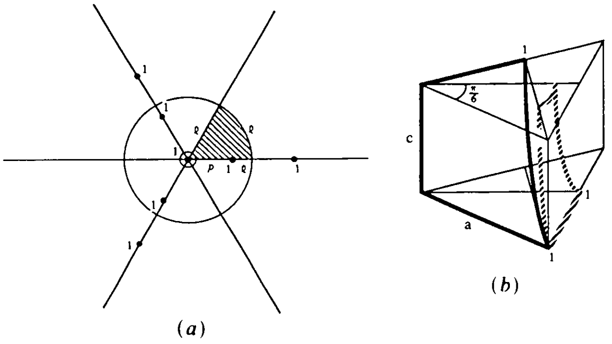

Fig. 12. The H′ and H surfaces.

Fig. 2(*a*) represents the only other possible regular branch-point distribution arising from the Schwarz case 4 tessellation, yielding a three-sheeted Riemann surface. This gives rise to the cubic I-WP surface, having genus 4, and the adjoint Stessman surface, which possesses self-intersections, illustrated in Fig. 2(*b*) (Schoen, 1970; Lidin, Hyde & Ninham, 1990). As opposed to the situation for the D and P surfaces, all reduced symmetry distortions of the I-WP surface lie outside the regular class of IPMS. This is apparent from Fig. 2(*a*): any spherical geodesic polygon generated by repeated reflection of the cubic I-WP polygon and bounded only by edges of a reduced-symmetry Schwarz tessellation produces an irregular distribution of the branch points assigned to it.

Fig. 9(*b*) is a general *Flächenstück* of the (one-parameter) tetragonal CLP family also discovered by Schwarz (1890). The family is imaged to itself under the adjoint transformation. The special case for which the equatorial branch points are evenly spaced corresponds to the fixed point of this transformation (illustrated in Fig. 3*a*). This CLP surface is the only one that is strictly self-adjoint.

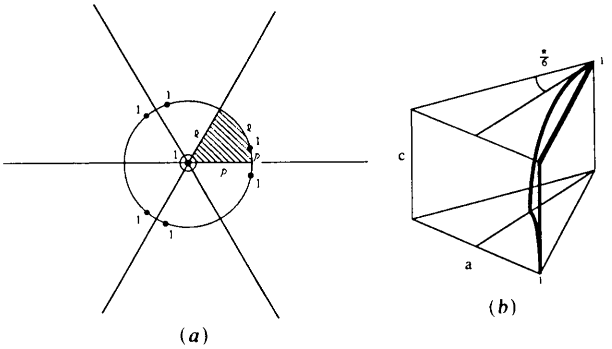

Fig. 13. The self-adjoint hCLP family.

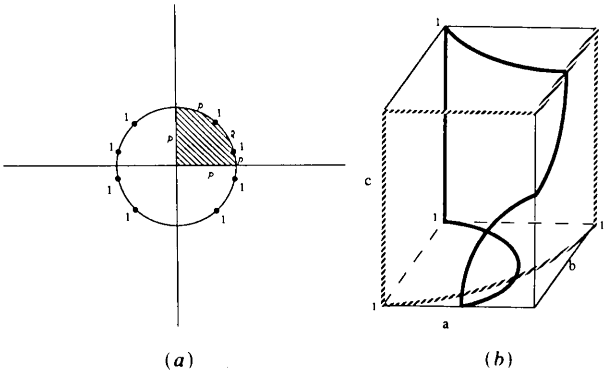

Fig. 15. The oCLP′ and oCLP surfaces.

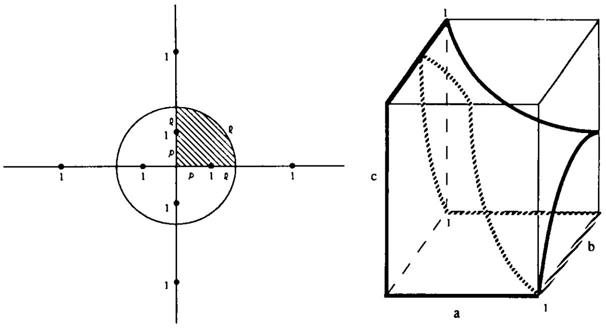

Fig. 14. The oDb and oPb surfaces.

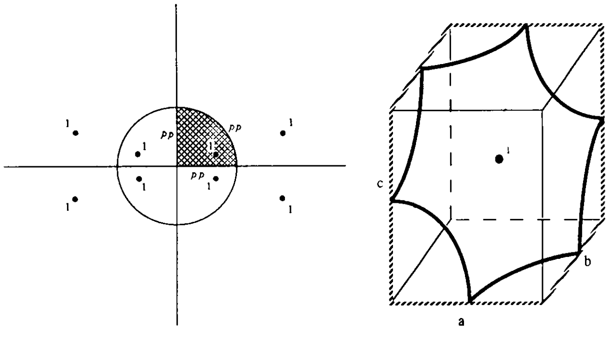

Fig. 16. The oPa and oDa surfaces.

Stretching of the bounding unit in either of the two horizontal directions breaks the symmetry of the branch-point distribution with respect to interchange of images of plane lines of curvature and linear asymptotes, displayed in Fig. 15(a). This reduction in symmetry introduces the distinction between the two-parameter families defining the general orthorhombic CLP surface and its adjoint (denoted oCLP′ and oCLP respectively), given in Fig. 15(b). Equivalently this distinction is evident from the two choices of parallelepiped unit bounding the tetragonal CLP surface. Again the double-sheeted Riemann surface implies a genus of 3 for these families.

The previously discovered IPMS remaining in this regular-class list are the genus 3 hexagonal surfaces (Lidin & Larsson, 1990). The *Flächenstück* of the one-parameter (hexagonal) hCLP family is shown in Fig. 13(b). By analogy with the tetragonal CLP case, the adjoint surface family replicates the original hCLP family, with the special member having an equally spaced branch-point distribution around the unit circle, displayed in Fig. 4(a), being precisely self-adjoint (up to reorientation). However, in contrast to the tetragonal case, hexagonal symmetry dictates that the hCLP family gives rise to self-intersections on repeated rotation. Similarly, the hexagonal surface family (denoted H′) illustrated by the solid-line circuit in Fig. 12(b) produces self-intersections on rotation. This is not the case though for the adjoint-surface family, with general *Flächenstücke* given by the broken-line circuit, which corresponds to the (hexagonal) H surface of Schwarz.

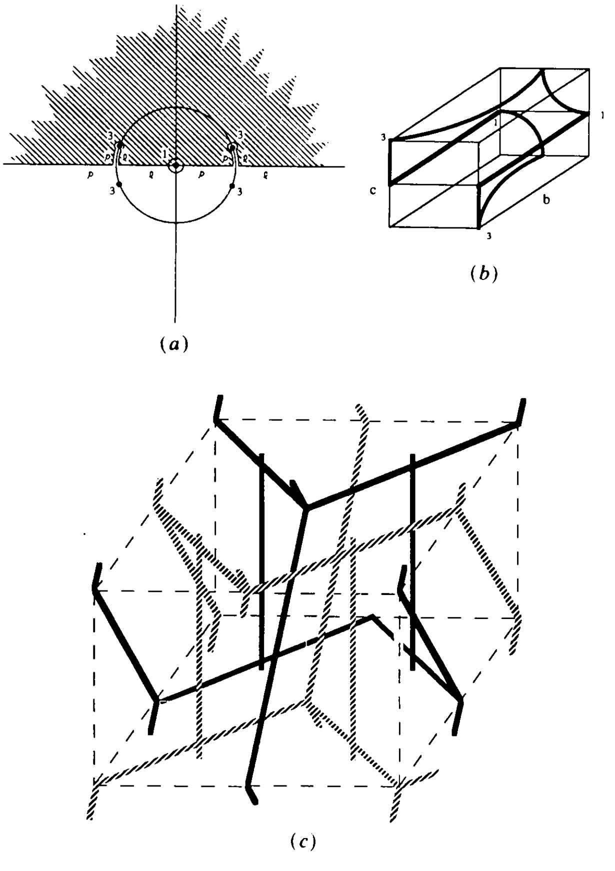

(a) (b) (c)

Fig. 17. The self-adjoint VAL surface. The labyrinth networks defined by this IPMS are illustrated in (c).

Of the other five regular branch-point distributions, which reduce to four since Fig. 7(a) is a special case of Fig. 17(a), one represents an intersection-free IPMS, two give IPMS with self-intersections while the remaining case possesses a noncrystallographic *Flächenstück*.

We now analyse these four new cases in detail. The branch-point distribution of Fig. 17(a) gives the one-parameter surface family with generic *Flächenstück* illustrated in Fig. 17(b). As the Riemann surface is four-sheeted, each member of the family is exactly self-adjoint (up to reorientation). On repeated reflection and rotation this *Flächenstück* generates an intersection-free IPMS of genus 5. We call this surface the V-shaped alternate layers (VAL) surface. The labyrinth networks defined by this IPMS consist of parallel (horizontal) layers of zigzag tunnels (alternately V-up and V-down), with alternate layers joined by a set of (vertical) straight tunnels running through the surface, as well as a set of oblique zigzag tunnels (Fig. 17c). Note that the branch-point distribution is invariant under the transformation $\omega \to -1/\omega$, that is, $b_1 = b_6 = 1$ and the third-order branch points have the property $\{-1/\omega_i\}_{i=2}^{5} = \{\omega_i\}_{i=2}^{5}$, hence the symmetry condition (23) is satisfied here for $\varphi = 0$. Further, the supplementary constraint (24) implies $\varphi = (\pi/3)(3-m)$ where $m = 0$, 1, 2, 3, thus $\varphi = 0$ is a solution, corresponding to $m = 3$. So in addition to the plane lines of curvature and linear asymptotes, the surface possesses a twofold rotation axis parallel to the y axis. This axis is hence parallel to, and lying midway between, the horizontal linear-asymptote pair in Fig. 17(b), and intersects the surface at the point with normal vector lying along this line, imaged at $\omega = i$. The fact that the surface defines a one-parameter family, as opposed to the general two-parameter orthorhombic surface cases discussed above, implies that only two dimensions of the bounding parallelepiped unit may be specified arbitrarily. This is apparent from Fig. 17(b) since the regularity criterion demands that the surface-normal vectors at the first-order flat points be vertical. Thus the generic orthorhombic VAL surface, for which this constraint is relaxed, lies outside the regular class and will be parametrized in a forthcoming study (Fogden, 1992). Fig. 7(a) represents the special case, possessing no additional symmetries, in which all edge lengths are coupled by the extra requirement that the normal vectors of the four third-order flat points are mutually perpendicular.

The new cases of Figs. 5 and 10 both produce self-intersecting hexagonal IPMS, denoted hI1 and hI2. Since the corresponding Riemann surfaces are three- and eight-sheeted, the genera of this pair of surfaces are four and nine, respectively (although the interpretation of genus in terms of the labyrinth networks is not so clear for self-intersecting IPMS). Note that in both cases the branch points reside on vertices of the Schwarz tessellation, so there are no degrees of freedom present in the resulting surfaces. In these cases the vertical edge length of the bounding hexagonal prism is coupled to the equilateral triangle dimension. Thus, as for the VAL surface, the generic hexagonal hI1 and hI2 surfaces are 'irregular'.

The distribution of Fig. 6(*a*) gives the *Flächenstück* illustrated in Fig. 6(*b*), which is exactly self-adjoint since the Riemann surface is four-sheeted, and represents the pentagonal analogue of the exactly self-adjoint special cases of the (tetragonal) CLP and (hexagonal) hCLP surfaces corresponding to Figs. 3(*a*) and 4(*a*). This surface is termed the pCLP surface. The general one-parameter pentagonal family, resulting from an arbitrary stretching of the bounding prism in the vertical direction, and analogous to the tetragonal and hexagonal families of Figs. 9(*b*) and 13(*b*), yields an irregular distribution of first-order branch points around the unit circle and thus again resides outside the regular class [and will be addressed in a forthcoming study (Fogden, 1992)]. While the unit sphere admits fivefold symmetry, this is not the case for the Euclidean space groups, thus the pentagonal CLP surface is noncrystallographic. Hence in this case no IPMS exists; continued reflection and rotation about the bounding mirror planes and twofold axes will produce self-intersections of arbitrarily high density in space, despite the fact that the corresponding Gauss-map image reproduces identical superpositions of the original Riemann surface. In the sense that this surface possesses normal-vector periodicity in the absence of any real-space periodicity (*i.e.* orientational order alone), it may represent a structure of physical interest and has been retained here.

There are other branch-point distributions derived from Table I2 that also satisfy the closure criterion on the Riemann surface but give rise to noncrystallographic minimal surfaces, the *Flächenstücke* of which are not illustrated here. In each case the distribution is symmetry-related by the composition of reflection in the unit circle and the internal symmetry axis $\arg \omega = \pi/2n$ of the Schwarz case 1 tile. In particular, the $n = 4$ solution $\{\Phi, \{1\}, \Phi\}$ of Table I2 yields the self-adjoint one-parameter family of catenoids bounded by coaxial square frames rotated by $\pi/4$ relative to each other.

Similarly the $n = 2$ solution $\{\Phi, \{1, 1\}, \Phi\}$ generates a *Flächenstück* and adjoint *Flächenstück* defining a pair of two-parameter surface families that are noncrystallographic generalizations of the one-parameter tD and tP families of Fig. 8(*b*). The new *Flächenstück* (together with its adjoint) is derived *via* double rotation (respectively reflection) of the tD (respectively tP) *Flächenstück* such that the composite symmetry of twofold rotation about the y axis followed by clockwise rotation of $\pi/2$ about the z axis is retained in the absence of the c-edge twofold axis (respectively c-face mirror plane). In particular, the adjoint *Flächenstück* gives the family of catenoids bounded by coaxial rectangles rotated by $\pi/2$ relative to each other. Just as the two distinct possible choices of parallelepiped bounding unit for the tD and tP surfaces yield two distinct orthorhombic derivative families in each case, there exists a second pair of noncrystallographic two-parameter derivative surface families possessing identical symmetries, generated by the $n = 2$ solution $\{\Phi, \Phi, \{1\}\}$. [Illustrations of the *Flächenstücke* for all three cases are given elsewhere (Fogden, 1991).] Note that, although these two pairs of surfaces are generically noncrystallographic, there is a countable infinity of special cases in which a translational unit containing only a finite number of surface self-intersections exists, corresponding to rational values of the rectangle edge-length ratio b/a.

3. Schwarz derivative tessellations

The above analysis exhausts 'regular' IPMS generated by tessellations of the sphere by Schwarz triangles. However, regular IPMS of lower symmetry occur that are inaccessible from these cases (for example, monoclinic surfaces). The complete set of such IPMS is obtained by extending the basis to all derivative tilings of those Schwarz cases that are consistent with the 'regularity' criterion, namely cases 1 (with polar angle π/n, $n \geq 2$), 2, 4 and 6 (Fogden & Hyde, 1992). The admission of derivative tilings only requires modification of the tessellation-counting arguments that lead to (I37) and yield the solutions listed in Table I2. The analysis of the distribution of images of plane lines of curvature and linear asymptotes on the Riemann surface and the various rotational-symmetry criteria are only specific to the regular class and apply to any underlying tiling.

(*a*) *Lunar tessellations*

In particular, consider a general member of the Schwarz case 1 family with polar angle π/n, $n \geq 2$. Its two basic derivative tilings are the Schwarz case 1 with the polar angle $2\pi/n$, obtained by deleting alternate rays, and the lunar tessellation with angle π/n *via* omission of the unit circle. For the former case the regularity criterion requires that n be even. Thus the first derivative type reproduces the original Schwarz case 1 family already exhausted above, with the addition now of the quadrant tiling $n = 2$ for which the polar angle is π. However, this quadrant tiling is equivalent, on reorientation, to the member $n=2$ of the latter derivative type. So, without loss of generality, the Schwarz case 1 derivative family is taken to be the lunar tessellations with angle π/n, $n\geq 1$.

Let $\{b_j\}_{j=1}^{2}$, $\{b'_k\}_{k=1}^{N'}$ and $\{b''_l\}_{l=1}^{N''}$ denote the orders of the branch points residing at the two polar vertices and on the edges and face, respectively, of a single lunar tile. The constraint (I10) on the complete distribution of branch points created by symmetry operations acting on the single lunar tile gives, on trivial modification of (I37), the condition

$$\frac{1}{n}\sum_{j=1}^{2}\frac{b_j}{b_j+1}+\sum_{k=1}^{N'}\frac{b'_k}{b'_k+1}+2\sum_{l=1}^{N''}\frac{b''_l}{b''_l+1}=\frac{4}{n} \qquad (25)$$

for the possible numbers and orders of branch points. For the degenerate hemispherical case $n=1$ there are no polar vertices and hence the first term is absent or, equivalently, is subsumed into the second term from the edge contributions.

Equation (25) possesses branch-point-set solutions $\{\{b_j\}_{j=1}^{2},\{b'_k\}_{k=1}^{N'},\{b''_l\}_{l=1}^{N''}\}$ for each integer n in the range $1\leq n\leq 8$. A decrease in the integer n, and hence the symmetry of the distribution, relaxes the constraints on the permissible range of branch-point orders and accordingly the number of such solutions increases in general. The solutions of (I37) for the Schwarz case 1 tessellation listed in Table I2 are recovered trivially here as the special cases in which the distribution is symmetry-related across the unit circle. Hence the solutions of (25) are naturally divided into the reduced-symmetry distributions derived from these Schwarz case 1 solutions and those distributions that possess no higher-symmetry analogues.

In this case too each branch-point set generates a number of surface families corresponding to the distinct assignments of branch points and symmetry operations to the pair of lune edges. The two possibilities for branch-point propagation are reflection over both edges or over one edge together with composition of reflection in the unit circle and the other edge. As noted previously, the latter possibility is only permitted by regularity if n is even, for which it is then equivalent to the composite symmetry operation of Schwarz case 1 with polar angle $2\pi/n$. As these have already been treated above, composite symmetry need only be addressed in the lunar case $n=2$ possessing no Schwarz-case analogue.

(*b*) *Special case*: *two-sheeted Riemann surfaces*

The complete set of solutions of (25) is too large to permit detailed consideration in this study. Analysis is limited here to those solutions consisting of (eight) order-one branch points. Each of these solutions is a reduced symmetry generalization of a Schwarz case 1 branch-point set listed in Table I2. Conversely, the solutions include all generalizations of IPMS discussed in the preceding section that have *Flächenstücke* containing eight order-one branch points, that reside in the regular class (that is, possess a double-sheeted Riemann surface) and that are consistent with lunar tessellations. Consequently, the closure criterion is automatically satisfied for these solutions as a reduction in symmetry preserves this property. For integers in the range $2<n\leq 8$, the allocations of order-one branch points to the lunar tiles, in accordance with (25), recovers the Schwarz case 1 solutions for each n value since the distribution is necessarily symmetric with respect to an origin-centred circle (which may be assumed, without loss of generality, to be the unit circle). Hence within the regular class the lunar tessellation generalizations are restricted here to the cases $n=2$ and $n=1$.

To determine all corresponding Weierstrass functions and classify the resulting surface symmetries, consider the generic branch-point distributions for these two cases. The $n=2$ case is the quadrant tessellation, defined by the great-circle pair with images the real and imaginary axes or, equivalently on reorientation, the real axis and the unit circle, in the complex plane. If both of the pair of lunar edges are reflection axes of the distribution then the set of images of a general point ω is the group

$$\langle\bar{\omega},-\bar{\omega}\rangle=\{\omega,\bar{\omega},-\omega,-\bar{\omega}\}$$

[with $\omega\in\mathbf{R}$ (respectively $i\mathbf{R}$) giving the degenerate-edge-case subgroup $\{A,-A\}$ where $A\in\mathbf{R}$ (respectively $i\mathbf{R}$)] or, with respect to the alternative orientation,

$$\langle\bar{\omega},1/\bar{\omega}\rangle=\{\omega,\bar{\omega},1/\omega,1/\bar{\omega}\}$$

[with edge cases $\{A,1/A\}$ if $\omega\in\mathbf{R}$ and $\{\exp(i\theta),\exp(-i\theta)\}$ if $|\omega|=1$]. Equations (6)–(10) imply that the segments of the real axis connecting neighbouring first-order branch points can be taken here as the images of alternate plane lines of curvature and linear asymptotes without loss of generality. Then, with respect to the first orientation, the same is true of the imaginary axis provided the tessellation vertices (at the origin and infinity) are unbranched points of the Riemann surface. This is also true of the unit circle in the second orientation if condition (19) is satisfied, that is, if the eight first-order branch points have the property

$$\prod_{i=1}^{8}\omega_i=1. \qquad (26)$$

By symmetry the branch points occur in pairs $\{\omega_i,1/\omega_i\}$, with the exception of the doubly degenerate case in which $\omega_i=\pm 1$. Hence (26) is trivially satisfied unless the two tessellation vertices are branch points of the Riemann surface. This confirms the fact that the surface properties are identical in the two orientations.

Now consider the other possibility for the $n=2$ lunar case, in which the symmetry operation of one of the edges is changed from reflection to the composite operation combining this with reflection in the internal-symmetry axis of the lune. For the first orientation, reflection in the real axis and composition of reflection in the imaginary axis and in the unit circle generates the group

$$\langle\bar{\omega}, -1/\omega\rangle = \{\omega, \bar{\omega}, -1/\omega, -1/\bar{\omega}\},$$

which reduces to the antipodal pair $\{A, -1/A\}$ if $\omega \in \mathbf{R}$. In the second orientation, reflection in the unit circle and composite reflection in the real and imaginary axes gives

$$\langle 1/\bar{\omega}, -\omega\rangle = \{\omega, 1/\bar{\omega}, -\omega, -1/\bar{\omega}\},$$

which degenerates to the antipodal pair $\{\exp(i\theta), -\exp(i\theta)\}$ if $|\omega|=1$. In the former the real axis is the image of a family of coplanar lines of curvature and/or normal asymptotic lines (meeting at right angles at first-order flat points) precisely as above, while the composite symmetry of the distribution corresponds to an additional twofold axis perpendicular to the surface and parallel to the linear asymptotes, provided $\varphi=0$ is a solution of (24), for $b=0$. This reproduces the above condition (26) here. In the latter orientation this condition ensures that the unit circle is the image of such a family of plane lines of curvature and linear asymptotes as before, with the composite symmetry now automatically imposing the additional twofold axis [since $\varphi'=\pi$ satisfies (13) for $b=0$ (and $\Delta\psi_r=0$)]. Here too the surface properties are identical with respect to the two orientations.

In summary then, we have two possibilities for the $n=2$ lunar case. Firstly, a perpendicular pair of branch-point reflection axes in the tiling produces a perpendicular pair of families of plane lines of curvature and/or linear asymptotes in the surface - provided the two tessellation vertices are unbranched points. Secondly, a single reflection axis combined with a composite reflection operation in the tiling yields a single such family, together with additional parallel twofold rotational symmetry, provided (26) is satisfied.

In the $n=1$ lunar case there exists only the possibility of a single reflection axis of the distribution. Taking this to be the unit circle, a general point ω possesses the image pair

$$\langle 1/\bar{\omega}\rangle = \{\omega, 1/\bar{\omega}\}$$

and the symmetry generates a single family of coplanar lines of curvature and/or normal asymptotic lines if the distribution obeys the constraint (26).

As opposed to the $n=2$ situation of perpendicular reflection axes, this constraint is not satisfied identically for a general $n=1$ distribution owing to the lack of second axis. So, as with the $n=2$ situation of composite reflection symmetry, (26) is nontrivial and is equivalent to the single real equation

$$\sum_{i=1}^{8} \arg \omega_i = 0 \pmod{2\pi} \qquad (27)$$

since unit-circle symmetry implies that the modulus of the product in (26) is unity. This constraint results from the fact that the symmetry operations $\omega \to 1/\bar{\omega}$ and $\omega \to -\omega$ generating these two cases only specify $\{\arg \omega_i\}_{i=1}^{8}$ up to an additive constant.

4. Regular-class solutions in this special case

The complete set of distinct families of eight first-order branch points generated by the lunar tessellations comprise fourteen distributions. There are three $n=2$ case distributions possessing a single reflection axis together with a composite reflection symmetry, illustrated in Figs. 18(*a*)-20(*a*) (with respect to the second orientation). The Weierstrass functions for each are the reciprocal square-rooted polynomials of degree eight obtained by inserting the set of branch-point sites $\{\omega_i\}_{i=1}^{8}$ into the form (I14). These are given, in terms of the unifying polynomial form consistent with this symmetry, in the correspondingly numbered rows 18-20 of Table 1. The $n=2$ lunar tessellation also yields six distributions having a pair of reflection axes, while there are five distinct $n=1$ solution families (possessing a single reflection axis only). Since these eleven cases give rise to generically non-crystallographic minimal surfaces, the details of them are not presented here [but may be found in an earlier study (Fogden, 1991)].

Again, the shaded region in Figs. 18(*a*)-20(*a*) represents the projected Gauss-map image of the *Flächenstück*, tiling the double-sheeted Riemann surface of the Weierstrass function. The plane lines of

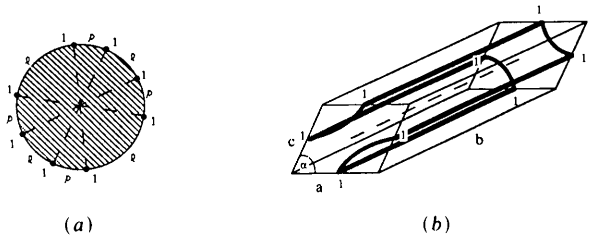

(*a*) (*b*)

Fig. 18. The self-adjoint mCLP family.

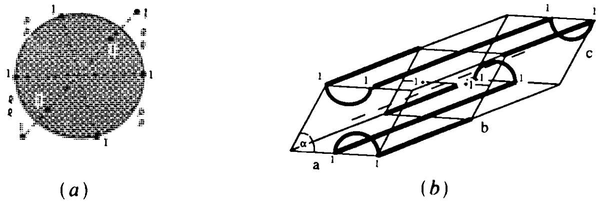

(*a*) (*b*)

Fig. 19. The self-adjoint mPD family.

curvature and/or linear asymptotes specifying each *Flächenstück* with respect to its generic bounding unit are illustrated in Figs. 18(*b*)-20(*b*). In the first two cases the adjoint-surface family replicates that of the original surface. The adjoint *Flächenstück* corresponding to Fig. 20(*b*) is, for clarity, illustrated separately in Fig. 20(*c*).

The *Flächenstück* image in Fig. 18(*a*) comprises the interior of the unit circle (*i.e.* hemisphere) on a single sheet of the Riemann surface, as it contains no branch points within. Reconstruction of the *Flächenstück* in Fig. 18(*b*) is straightforward since it is bounded by a circuit of plane lines of curvature and linear asymptotes (as was the case for each of the Schwarz-tiling examples discussed above). However, the situation is more complicated for Figs. 19 and 20. In Fig. 19(*a*), the image consists of two superposed copies of the unit-circle interior pinned together at the branch points. On winding once around a pair of branch points of first order, we form a (continuous) closed loop on the Riemann surface. Thus, in contrast to the situation in Fig. 16(*a*), the boundary of the *Flächenstück* image here comprises two disjoint circuits, corresponding to the two disjoint bounding-curve segments in Fig. 19(*b*). The endpoints of each curve segment are thus identical up to a lattice translation (to which the Weierstrass representation is invariant). The two halves of the *Flächenstück* are related by the twofold axis perpendicular to the surface. The *Flächenstücke* of Figs. 20(*b*) and 20(*c*) may be similarly derived from Fig. 20(*a*).

These *Flächenstücke* generate three-parameter families of surfaces, possessing a set of coplanar lines of curvature and/or normal asymptotic lines together with a parallel internal twofold axis, by virtue of the additional constraint (27) on the distributions of Figs. 18(*a*)-20(*a*). Hence they represent monoclinic distortions of the two-parameter orthorhombic families (given by the distributions of eight first-order branch points symmetric with respect to reflection in the three edges of the Schwarz case 1, $n = 2$ tessellation). Compared to the related orthorhombic IPMS, these monoclinic IPMS lack a perpendicular intersecting pair of plane lines of curvature and/or linear asymptotes but retain the twofold axis produced on composition.

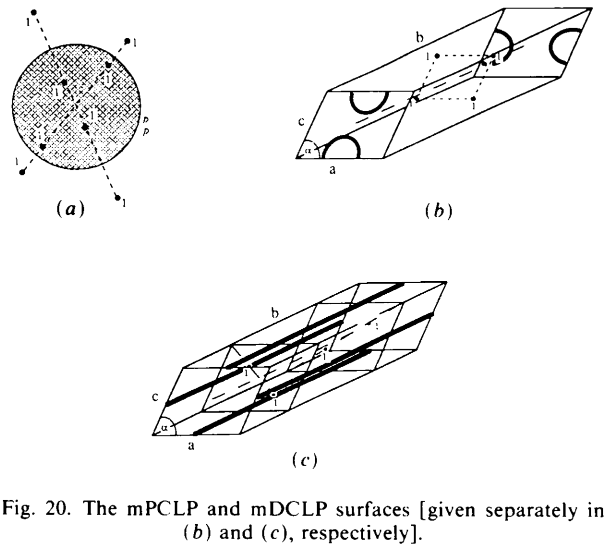

(*a*) (*b*) (*c*)

Fig. 20. The mPCLP and mDCLP surfaces [given separately in (*b*) and (*c*), respectively].

In particular, for the oDb and oPb *Flächenstücke*, loss of the *c*-edge linear asymptote and the *c*-face plane line of curvature of Fig. 14(*b*), respectively, together with the corresponding curves along the (*a* or) *b* edge and face in both cases, gives the monoclinic surface element of Fig. 19(*b*). This distortion removes the distinction between the orthorhombic surface and its adjoint, hence the resulting three-parameter family (denoted here the mPD surface) is self-adjoint.

Alternatively, loss of both the *a*- and *b*-edge (and face) symmetries in this pair, or equivalently the *a*- and *b*-edge (respectively face) symmetries of the oDa (respectively oPa) *Flächenstück* of Fig. 16(*b*), yields a distinct monoclinic derivative surface pair illustrated in Figs. 20(*c*) and (*b*). This pair of monoclinic families is likewise obtained from the orthorhombic CLP pair, of Fig. 15(*b*), by removing the (*a*- or) *b*-edge (respectively face) symmetry of the oCLP surface (respectively oCLP′ surface) together with those of the *c* edge and face in both cases. Consequently, these surfaces are denoted mDCLP and mPCLP respectively. Further, loss of the *a*- and *b*-edge (respectively face) symmetries in these two cases produces the self-adjoint monoclinic CLP family ('mCLP' surfaces) in Fig. 18(*b*).

To summarize these relations, recall that the D, P and CLP surfaces all possess a single one-parameter tetragonal family, each giving rise to a pair of two-parameter orthorhombic families. The monoclinic distortion now produces four three-parameter families. Specifically, the D pair merges with the oCLP surface to yield the common mDCLP surface (with the adjoint transformation of this operation supplying the mPCLP surface from the P pair and the oCLP′ surface). Further, the two adjoint pairs oCLP–oCLP′ and oDb–oPb produce their own self-adjoint monoclinic relatives mCLP and mPD, respectively.

For the other eleven distributions of eight branch points (of first order) related to the lunar tessellations, the number of degrees of freedom dictated by the symmetry of the distribution exceeds that of the corresponding crystallographic system in $\mathbf{R}^3$. In this sense these cases deviate from all those considered above. Although the symmetry elements defining the generic *Flächenstücke* produce noncrystallographic minimal surfaces, the imposition of constraints on the distribution (reducing the number of degrees of freedom to that compatible with the crystal unit) may give rise to IPMS subclasses.

As an example, consider the above-mentioned six distributions related by reflection across both edges of the $n = 2$ lunar tiling. The associated *Flächenstücke* represent four-parameter surface families possessing perpendicular pairs of coplanar lines of curvature and/or normal asymptotic lines and are reduced-symmetry generalizations of Schwarz case 1 surfaces. If the four independent dimensions characterizing the *Flächenstück* with respect to its bounding cell may be constrained such that the symmetry elements are (nontrivially) locked into crystallographic positions then a new orthorhombic IPMS results. In particular, for one of these six cases this procedure yields an orthorhombic IPMS family encompassing both the oPb and H surfaces.

The introduction of such additional constraints is again a manifestation of the fact that orientational order is not always sufficient to ensure translational order. These extra conditions are strictly global and necessarily involve contour integration of the generic Weierstrass functional form *via* the representation (I1). As they cannot be derived from consideration of the Gauss map alone, they lie outside the scope of the present study. However, we briefly illustrate their application in analysing the terminal stage in symmetry reduction of the D, P and CLP surfaces within the regular class - the triclinic distortions of the monoclinic *Flächenstücke* of Figs. 18(*b*), 19(*b*) and 20(*b*), (*c*).

5. Triclinic IPMS

We first reanalyse monoclinic symmetry to relate it to its triclinic counterpart. The Gauss-map symmetry $\omega \rightarrow 1/\bar{\omega}$ (*i.e.* reflection in the unit circle) corresponds to a line of curvature in the xy plane (positive sign) and an asymptote along the z axis (negative sign) provided equation (I23) is satisfied for $n_1 = n_2 = 0$, that is,

$$(1/\omega^4)\bar{R}(1/\bar{\omega}) = \pm R(\omega). \qquad (28)$$

As noted above, this reduces on substitution of the functional form (I14) or (I15) to the constraint (19) for the positive root, with the sign of the right-hand side in turn reversed for the negative root. Similarly, the symmetry $\omega \rightarrow -\omega$ (*i.e.* reflection in the origin) yields twofold perpendicular rotational symmetry about the point on the surface with normal vector parallel to the z axis provided $\varphi' = \pi$ is a solution of (12), that is,

$$R(-\omega) = R(\omega), \qquad (29)$$

which, again as stated previously, is satisfied identically here. Composition of these two operations implies the symmetry $\omega \rightarrow -1/\bar{\omega}$ of the Gauss map on reversal of the surface-normal-vector orientation (*i.e.* inversion in the origin). This generates an off-surface centre of inversion symmetry if $\varphi'' = 0$ satisfies (16), *i.e.*

$$(1/\omega^4)\bar{R}(-1/\bar{\omega}) = R(\omega), \qquad (30)$$

which again recovers the constraint (19). Hence off-surface inversion symmetry exists in the monoclinic case if the Weierstrass function satisfies at least the positive root of (28) or, equivalently, if the surface possesses at least plane lines of curvature.

This confirms the geometrically obvious fact that the surfaces of Figs. 18(*b*), 19(*b*) and 20(*b*) display off-surface inversion about the intersection of the internal twofold axis with the mirror planes, that is, about the centres of the endface pair. This is not the case however for the adjoint *Flächenstück* of Fig. 20(*c*) since it possesses linear asymptotes parallel to the additional twofold axis in the absence of any plane lines of curvature. In all cases each first-order branch point corresponds to an on-surface inversion centre as $\varphi''' = 0$ satisfies (20) since $\exp(i\psi_r) = -1$ here - a property common to all Weierstrass functions with double-sheeted Riemann surfaces.

On triclinic distortion of a monoclinic IPMS the set of coplanar lines of curvature and/or normal asymptotic lines are lost, together with the internal twofold axis, while any existing off-surface inversion centres produced on composition of these original symmetries are retained. Hence the triclinic IPMS differ from all others in this study in possessing Gauss maps devoid of any underlying tessellation structure. The branch-point distribution only has the symmetry $\{-1/\bar{\omega}_i\}_{i=1}^{8} = \{\omega_i\}_{i=1}^{8}$, subject to the associated constraint (19) for this on-surface inversion, reducing as noted above to the condition (26) or (27) here [which is common to both the positive and negative root of (28) by virtue of the two-sheeted Riemann surface]. Hence the generic triclinic regular-class Weierstrass functional form is

$$R(\omega) = \left(\prod_{i=1}^{4} (\omega - \omega_i)(\omega + 1/\bar{\omega}_i)\right)^{-1/2} : \quad \prod_{i=1}^{4} (-\omega_i/\bar{\omega}_i) = 1, \qquad (31)$$

or equivalently on expansion,

$$R(\omega) = \left(\sum_{m=0}^{8} \alpha_m \omega^m\right)^{-1/2} : \alpha_m = (-1)^m \bar{\alpha}_{8-m}, \quad \alpha_0 = \alpha_8 = 1. \qquad (32)$$

The functional form (31) or (32) contains seven free real variables and thus gives rise to a seven-parameter noncrystallographic surface family. The most general triclinic unit only has five degrees of freedom (up to a uniform dilation) given by the variable edge-length ratios a/c and b/c and shear angles α, β, γ. Hence at least two real constraints must be imposed on the generic form to yield a triclinic IPMS family. These constraints derive from the crystallographic requirements of triclinic symmetry regarding the relative positions of the off- and on-surface inversion centres. With reference to the triclinic cell of Fig. 21, the distortions of the mCLP, mPD and mPCLP *Flächenstücke* [shown in Figs. 18(*b*), 19(*b*) and 20(*b*)] possess off-surface inversion symmetry at the endface centres of this unit, denoted B_1 and B_2. These three cases then represent the three distinct possible allocations of the eight first-order branch points (on-surface inversion centres) to the remaining face-centre and edge-midpoint sites.

The first such possibility positions branch points at the edge midpoint sites A_1, A_2, A_3, A_4, with the remaining four positions then specified by off-surface inversion to be the antipodal edge midpoints A'_1, A'_2, A'_3, A'_4. Hence for the triclinic distortion of the mCLP *Flächenstück* of Fig. 18(*b*) the relative position vectors $\mathbf{B}_1\mathbf{B}_2$, $\mathbf{A}_1\mathbf{A}_2$ and $\mathbf{A}_3\mathbf{A}_4$ of the off-surface centres and the branch-point pairs must be equal,

$$\mathbf{A}_1\mathbf{A}_2=\mathbf{A}_3\mathbf{A}_4=\mathbf{B}_1\mathbf{B}_2. \tag{33}$$

The second possibility, corresponding to one half of the bounding unit of Fig. 19(*b*), again contains branch points at the edge midpoints A_1, A_2 (and the antipodal pair A'_1, A'_2), and now a further pair at the face centres B_3, B_4 (with off-surface inversion images B'_3, B'_4 at the parallel face centres of the adjacent unit). In this distorted mPD *Flächenstück* the three relative position vectors $\mathbf{B}_1\mathbf{B}_2$, $\mathbf{A}_1\mathbf{A}_2$ and $\mathbf{B}'_3\mathbf{B}_4$ must now be identical,

$$\mathbf{A}_1\mathbf{A}_2=\mathbf{B}'_3\mathbf{B}_4=\mathbf{B}_1\mathbf{B}_2. \tag{34}$$

The final possibility, derived from one quarter of the unit in Fig. 20(*b*), has branch points at the four face centres B_3, B_4, B_5, B_6 (again with images B'_3, B'_4, B'_5, B'_6 occupying the corresponding sites of the adjoining cell). Hence for the distorted mPCLP *Flächenstück* (Fig. 20*b*) common to the P and CLP families, the triple $\mathbf{B}_1\mathbf{B}_2$, $\mathbf{B}'_3\mathbf{B}_4$ and $\mathbf{B}'_5\mathbf{B}_6$ must be equal,

$$\mathbf{B}'_3\mathbf{B}_4=\mathbf{B}'_5\mathbf{B}_6=\mathbf{B}_1\mathbf{B}_2. \tag{35}$$

The description of these three cases is thus unified by the triclinic constraint that the relative position vector of the off-surface inversion centres coincides with those of two pairs of flat points. As the functional form (31) is symmetric with respect to the ω_i, the surface-normal-vector images of these two pairs may be assumed, without loss of generality, to be ω_1, ω_2 and ω_3, ω_4. Substitution of the representation (I1) then gives

$$\operatorname{Re}\left\{\int_{\omega_1}^{\omega_2}[1-\omega'^2,\, i(1+\omega'^2),\, 2\omega']R(\omega')\,\mathrm{d}\omega' - \int_{\omega_3}^{\omega_4}[1-\omega'^2,\, i(1+\omega'^2),\, 2\omega']R(\omega')\,\mathrm{d}\omega'\right\}=0, \tag{36}$$

supplying, in general, three real constraints on the branch-point distribution.

Hence the triclinic 'regular' IPMS families possessing eight first-order flat points with distinct normal vectors are generated by the Weierstrass function (31) or (32) subject to the constraints (36). If the system of three equations (36) is nondegenerate then the surfaces are accordingly reduced to four-parameter families, having one less degree of freedom than the general triclinic symmetry class. In this case these regular IPMS can only access a subset of the full triclinic space. This is plausible since the assumption of regularity is certainly a limitation (for example, all first-order branch points must be inversion centres).

As the triclinic distortions of the mCLP, mPD and mPCLP surfaces are specified identically, with no underlying tessellation to distinguish symmetrically different branch-point configurations, they are effectively merged into one continuous IPMS family. The triclinic distortion of the fourth possible monoclinic IPMS, the mDCLP surface, given by the adjoint *Flächenstück* in Fig. 20(*c*) (lacking any off-surface inversion symmetry), is simply derived from that of Fig. 20(*b*) on multiplication of the functional form by the complex constant *i*. Conversely, the monoclinic cases may be recovered as the trivial solutions of (36) on imposition of the additional symmetries $\omega\to 1/\bar{\omega}$ and $\omega\to -\omega$.

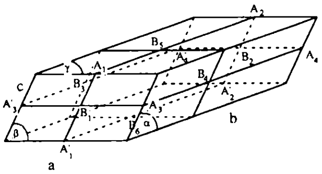

Fig. 21. A general triclinic unit cell. The symbols label edge midpoints and face centres that are possible points of inversion for the triclinic IPMS discussed in § 5.

6. Concluding remarks

This work was motivated by our lack of knowledge of bicontinuous forms. Although many IPMS have been found, to date there has been no systematic procedure for generating them. This work attempts to redress that imbalance: we have presented an algorithm for the enumeration (and parametrization) of all IPMS within the regular class. All such IPMS related to Schwarz triangle tilings have been given here. This listing is only incomplete in respect of the IPMS derived from lunar tilings (for which the analogous conditions have been detailed and some representative examples analysed). Completion of this task is straightforward, albeit tedious. The minimal surfaces described and parametrized in this paper are displayed in Table 2. In particular, six new intersection-free IPMS (the oCLP′, VAL, mCLP, mPD, mPCLP and mDCLP surfaces) have been determined.

For IPMS in the regular class the explicit calculation of surface coordinates, *via* numerical integration of the Weierstrass representation, is readily performed. As each of the s branches of the Weierstrass function only differs by a constant factor $\exp(i\psi_p)$, the traversal of the Riemann surface induced in such a calculation is easily traced. Numerical generation of the *Flächenstück* is extremely useful in visualizing the lower-symmetry examples in which the plane lines of curvature and/or linear asymptotes do not define a boundary circuit. Even in higher-symmetry cases the computation is worthwhile since the interpenetrating labyrinth networks partitioned by the IPMS are not always immediately apparent.

The technique we have used also leads naturally to nonclassical minimal surfaces that are orientationally ordered but lack translational symmetry. Whether these surfaces are physically relevant remains to be seen. However, the recent interest in quasicrystalline structures and orientational order warrants there inclusion here. We have looked for surfaces whose point-group symmetries are those of the icosahedron, since these are allowed symmetries on the sphere, however, no such minimal surface exists within the regular class. (Note that such an icosahedral surface does exist as an irregular surface, of higher genus.) However, special positions on one of these new noncrystallographic surfaces, the pentagonal CLP surface, exhibits the same point-group symmetry as that of the so-called T-phases in rapidly quenched alloys (Bendersky, 1985). This symmetry has also been observed in a lyotropic liquid crystal (Fontell, 1991).

Having concluded our study of the regular class of IPMS, the question of possible extension of the construction algorithm to all IPMS arises. The recognition of this special class is a somewhat arbitrary one, introduced for the sake of simplicity of the Riemann-surface structure of the Weierstrass function, thus facilitating an exhaustive listing of all such possible surfaces. This listing serves a dual purpose - firstly, in unifying all previously discovered IPMS (*e.g.* D, P and CLP surfaces) within a systematic parametrization scheme that permits generalization to reduced-symmetry families and isolating new IPMS such as the VAL surface illustrated in Fig. 17(b) and (c) and, secondly, in the converse statement that there exists no other IPMS in this class. However, the limitations of this class are clear, both from the existence of 'irregular' IPMS, such as the Neovius [or C(P)] surface, and from the existence of 'regular' IPMS, such as the I-WP surface, which pass into the irregular class on crystallographic distortion. The construction framework of topological, geometrical and Riemann surface features established here permits a natural generalization of the above to the irregular class. This is addressed in a forthcoming study (Fogden, 1992).

References

BENDERSKY, L. (1985). *Phys. Rev. Lett.* **55**, 1461.

FISCHER, W. & KOCH, E. (1989). *Acta Cryst.* A**45**, 726-732.

FOGDEN, A. (1991). PhD thesis, Australian National Univ., Canberra, Australia.

FOGDEN, A. (1992). Submitted to *Acta Cryst.* A.

FOGDEN, A. & HYDE, S. T. (1992). *Acta Cryst.* A**48**, 442-451.

FONTELL, K. (1991). Private communication.

LIDIN, S. (1988). *J. Phys. (Paris)*, **49**, 421-427.

LIDIN, S. & HYDE, S. T. (1987). *J. Phys. (Paris)*, **48**, 1585-1590.

LIDIN, S., HYDE, S. T. & NINHAM, B. W. (1990). *J. Phys. (Paris)*, **51**, 801-813.

LIDIN, S. & LARSSON, S. (1990). *J. Chem. Soc. Faraday Trans.* **86**, 769-775.

SCHOEN, A. H. (1970). *Infinite Periodic Minimal Surfaces Without Self-Intersection. NASA Tech. Note* No. D-5541.

SCHWARZ, H. A. (1890). *Gesammelte Mathematische Abhandlungen.* Berlin: Springer.

Acta Cryst. (1992). A**48**, 591-595

Reciprocity in Electron Diffraction

BY JAMES GUNNING AND P. GOODMAN

School of Physics, University of Melbourne, Parkville, Victoria 3052, *Australia*

(*Received* 2 *August* 1991; *accepted* 11 *February* 1992)

Abstract

The symmetry of reciprocity is reviewed in the context of relativistic quantum mechanics with the specific aim of relating to C, P and T invariances. From this investigation global time reversal is found to be a sufficient condition for reciprocity to hold in scattering from a vector potential. The present proof is free from assumptions of small-angle scattering and from restrictions on z-dependent terms in the scattering equation, and by avoiding S-matrix theory is thought to be accessible to undergraduate teaching.

0108-7673/92/040591-05$06.00

© 1992 International Union of Crystallography